Midlatitude Temperature Variations in the Oligocene to Early Miocene

José Guitián[1] [iD], Samuel Phelps[2] [iD], Pratigya J. Polissar[2] [iD], Blanca Ausín[1] [iD], Timothy I. Eglinton[1] [iD], and Heather M. Stoll[1]

[1]Geological Institute, ETH Zürich, Zürich, Switzerland, [2]Lamont-Doherty Earth Observatory, Columbia University, Palisades, NY, USA

Abstract Antarctic ice sheet margin extent and the sensitivity of benthic $\delta^{18}O$ to orbital forcing have varied on million-year timescales during the Oligocene to Early Miocene. However, few sea surface temperature (SST) records for this time interval exist to evaluate links between polar processes and mean temperature outside polar regions. Here, we present a new record of SST for the time interval 30 to 17 Ma derived from the long-chain alkenone unsaturation ratio ($U_{37}^{k'}$) at Integrated Ocean Drilling Program Site 1406A in the midlatitude North Atlantic. Results confirm that warm temperatures from 24°C to over 30°C prevailed in midlatitudes in this time and suggest a transition from colder early-middle Oligocene to warmer average conditions after 24.5 Ma. The global significance of this transition is highlighted by the coincidence with changes in the dominance from marine- to terrestrial-terminating ice sheets in the Ross Sea around Antarctica. The longest continuous section of the record (20.6 to 26.6 Ma) contains multiple 2 million-year cycles in SST, potentially paced by long obliquity modulation. Complex and temporally varying relationships are observed between North Atlantic SST and benthic $\delta^{18}O$ in paired samples; significant covariation is only observed around the Oligocene-Miocene transition, coincident with a lower average marine ice extent. These North Atlantic $U_{37}^{k'}$ temperature records provide a new context in which to examine the stability of climate and the Antarctic ice sheet during the Oligocene and early Miocene.

1. Introduction

Over the Cenozoic, global climate transitioned progressively from a "greenhouse Earth" with ice-free poles and shallow latitudinal temperature gradient to an "icehouse Earth" with the emplacement of polar ice sheets first on the Antarctic continent and subsequently in the Northern Hemisphere (Deconto et al., 2008; Pälike et al., 2006; Zachos et al., 2001). This transition has not been linear: Since the late Eocene, climate has likely been characterized by both orbital scale and multimillion-year secular oscillations superimposed on the long-term cooling. Increased temporal resolution of benthic oxygen isotopic records and recent Antarctic ice margin records have both revealed significant orbital modulation of the extent of the large East Antarctic Ice sheet throughout the Oligocene and Miocene, with a behavior potentially modulated by long obliquity (2.2 Myr) cycles (De Vleeschouwer et al., 2017; Gasson et al., 2016; Levy et al., 2016; Levy et al., 2019; Liebrand et al., 2017). Shelfal sequences in Australia also show orbtially paced ±25m sea level variations interpreted as significant Antarctic ice sheet variability in the early Oligocene (Gallagher et al., 2013). This dynamic ice sheet behavior may be due to warm high-latitude temperatures, which allowed both high moisture transport to the ice sheet and more dynamic ablation processes; however, few constraints exist on high-latitude temperatures during this time interval.

The variability and evolution of surface temperature during the Oligocene and early Miocene is not well characterized. In contrast to the late Miocene, where over a dozen globally distributed temperature records from alkenone unsaturation ratios ($U_{37}^{k'}$) record pronounced midlatitude and high-latitude cooling (Herbert et al., 2016), absolute sea surface temperature (SST) estimates for the Oligocene to early Miocene are very limited in time and spatial extent. One late Eocene through Oligocene temperature record from $U_{37}^{k'}$ in north Atlantic sediments suggests temperatures averaging 26 °C (Liu et al., 2018). The TEX_{86} temperature proxy based upon glycerol dialkyl glycerol tetraethers (GDGTs) was used to reconstruct temperatures for the last 40 Myr in the tropical and high-latitude North Atlantic Ocean (Super et al., 2018; Zhang et al., 2013). These high-latitude North Atlantic TEX_{86} temperatures are warmer than coeval $U_{37}^{k'}$-derived temperatures

from lower latitudes in the western equatorial Atlantic, and it is unclear if the difference was a real feature of Oligocene climate or a result of different proxies used in each site.

Uniquely, despite the large documented orbital scale variability in benthic $\delta^{18}O$, only one Oligocene to Miocene SST record has been coupled to $\delta^{18}O$ of benthic foraminifera (Super et al., 2018). Given the orbital scale variability in benthic $\delta^{18}O$ and potentially in SST in higher latitudes, aliasing of lower resolution long-term temperature trends is a risk and might be relating extreme orbital cycle timing. Referencing surface temperature records to benthic foraminiferal $\delta^{18}O$ reduces the risk of aliasing by allowing assessment of what part of the orbital cycle is sampled. In addition, coupled surface temperature and benthic $\delta^{18}O$ allow assessing whether surface temperature variability is correlated to high-latitude temperature and ice volume signals in benthic $\delta^{18}O$.

Here, we present a new SST record from Integrated Ocean Drilling Program (IODP) Site 1406A, on the Newfoundland margin, for the early Oligocene to Miocene time interval. The clay-rich sediments host abundant biomarkers and excellent microfossil preservation. We focus on temperature estimates from the alkenone undersaturation index, because these biomarkers from haptophyte algae must be produced in the euphotic zone and therefore closely linked to SSTs. Our temperature record is coupled to paired benthic foraminifera $\delta^{18}O$ and $\delta^{13}C$ determinations from the same sediments, allowing us to evaluate the link between midlatitude SST and the high-latitude temperature and ice volume components in the benthic $\delta^{18}O$ values. The temperature record is qualitatively compared with the abundance of the calcareous nanno-fossil *Helicosphaera* spp., of subtropical affinity (Bralower, 2002; Gard & Backman, 1990; Marino et al., 2014; Tremolada & Bralower, 2004), which is also sensitive to temperature. To evaluate the constancy of the depositional regime of these sediments, we also present the sortable silt grain size, since faster currents tend to deposit a higher percentage of coarser particles, while slow velocity currents will allow fine sediment to settle. Finally, to assess the degree to which temperature estimates from different proxies are comparable, for a subset of samples, we have also measured TEX_{86} temperatures from Site 1406A, although TEX_{86} derived temperatures are potentially subject to a greater range of uncertainties, including the significance of production in or below the thermocline (Ho & Laepple, 2016; Hurley et al., 2018; Zhang & Liu, 2018) temporal variation in the production depth (Schmidt et al., 2018), potential seasonal bias and the ecological or community specific effects (Polik et al., 2018), and contribution of GDGTs from terrestrial environments. Together, these new climatic and environmental records from Site 1406A clarify the behavior of contrasting proxies and allow confident resolution of million-year timescale temperature trends through the Oligocene and early Miocene.

2. Methods

2.1. Site and Sediments

Off the southeast coast of Newfoundland, Canada (Figure 1), the IODP Expedition 342 recovered Paleogene to Neogene sedimentary sequences with an exceptionally high accumulation rate and very good preservation of microfossils due to the high clay content (Norris et al., 2014). Most of the sequences are part of a contourite drift deposits (Faugères et al., 1999; Rebesco et al., 2014; Stow et al., 2002) that exceed 2,000 m in thickness and extend over hundreds of km (Boyle et al., 2017). Seismic stratigraphy has revealed that the flow con-toured the ridges of Newfoundland since the middle Eocene, characterized by deep and slightly more intense current after the Late Oligocene (Boyle et al., 2017). During the Oligocene to early Miocene, time interval seismic data show muddy drift separated by an eroded horizon.

In this study we focus on sediments from 30 to 17 Ma from Site 1406 Hole A (40°21.0′N, 51°39.0′W; 3,814 m below sea level [bsl]) drilled on the J-Anomaly Ridge drift. The age model between 30 to 27 Ma and 19 and 17 Ma is based on shipboard biostratigraphy (Norris et al., 2014). Between 27 and 19 Ma, chronology is based on revised detailed bioevents and magnetostratigraphy; ages have lower uncertainty during this interval [Van Peer, Xuan, et al., 2017]. The age-modeling software Bacon (Blaauw & Christen, 2011) was used to calculate ages from CSF-A depths to ages [Van Peer, Liebrand, et al., 2017] (Figure 2). All ages are adjusted to the Geologic Time Scale 2012 (Gradstein et al., 2012). On this timescale, two ~2-Myr-long hiatuses were interpreted: a glauconite event within the 21- to 19-Ma interval [Van Peer, Xuan, et al., 2017] and a slump around 27-29 Ma (Norris et al., 2014), which corresponds with an identifiable seismic horizon. The largest uncertainty on this chronology appears at 27.4 m (CSF-A), 19.1 Ma with a moderate 965-kyr-wide 95%
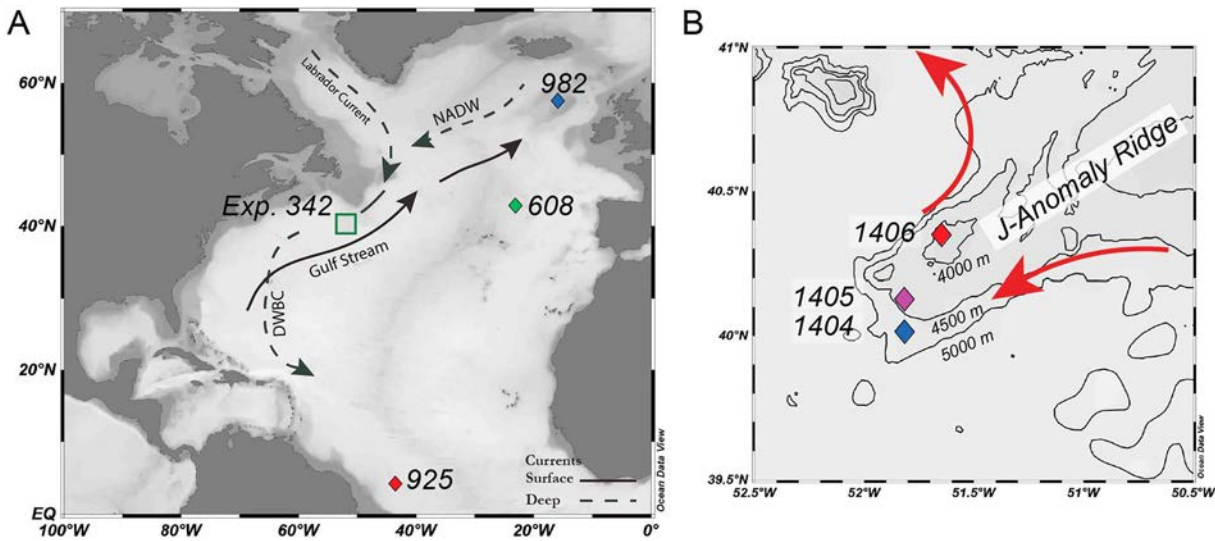
Figure 1. (a) Symbols show modern locations of Expedition 342, Ocean Drilling Program and Integrated Ocean Drilling Program Sites discussed on the text and arrows main current directions. The solid and dashed arrows show modern surface and deep currents respectively. (b) Expedition 342 sites discussed located over the J-Anomaly Ridge drift at different depths. The red line illustrate modern Deep Western Boundary Current core path.

confidence interval. In addition, two samples from Site 1405 Hole A (4287 m bsl) were examined where shipboard magnetostratigraphy allowed precise correlation to Site 1406A. The youngest 1405A sample corresponds to 23.03 Ma chron boundary C6Cn.2n/C6Cn.2r, while the oldest corresponds to the base of *Paragloborotalia pseudokugleri* zone at 25.21 Ma. The paleolatitude of Exp. 342 sites does not differ significantly from their modern latitude due to the polar location of the rotation pole of the mid-Atlantic ridge, which led to a longitudinal rather than poleward, tectonic migration of the Newfoundland banks, attaining a position of 41°N, 46°W by 18 Ma (Liu et al., 2018).

Today, surface oceanography is influenced by the eastern branch of the Gulf Stream that flows west-northeast transporting warm waters to the east north Atlantic (Schmitz & McCartney, 1993). Due to the current, today, the 10°C mean annual temperature isotherms progress from 43°N in the west Atlantic to 60°N in the east Atlantic, although the difference in latitude of the 15°C isotherm is more similar, 41°N and 45°N in the west and east, respectively (World Ocean Atlas 2013; https://odv.awi.de/data/ocean/). The modern deep oceanographic configuration is marked by cold water masses sourced in high latitudes.
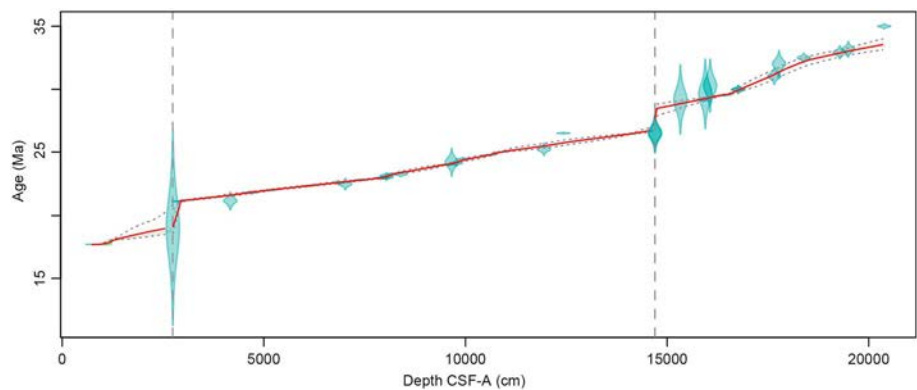
Figure 2. Age-depth model for Site 1406 Hole A. Panel shows the calibrated age tie points with associated error (transparent blue). All but one radiolarian event (*Lychnocanoma elongata*) were excluded from the calibration due to the large uncertainties and contradictions with revised magnetostratigraphy[Van Peer, Xuan, et al., 2017]. The vertical lines indicate hiatus positions. The envelope defined by gray dashed lines shows 95% confidence interval, and the red curve is the best estimation model based on the mean age for each depth.

The Deep Western Boundary Current, continuation of the Labrador Sea Water, join immediately north of the Newfoundland shelf and flow southwest, parallel to the American coast at 3,500- to 4,500-m paleodepths (Hall et al., 2013; McCave & Tucholke, 1986; Rhein et al., 2015), as part of the North Atlantic Deep Water (Schmitz & McCartney, 1993). Debate remains on the onset of these ocean circulation patterns. Tectonic adjustment across in subarctic seas during the latest Eocene might have triggered first ancient Northern Component Water (Coxall et al., 2018). However, northeast Atlantic contourite sediment drifts place the origin even earlier at the middle Eocene (Hohbein et al., 2012).

2.2. Organic Geochemistry for SST Reconstruction

A total of 42 samples from Site 1406A and 4 from Site 1405A were analyzed. A total lipid extract was obtained from 20-40 g of freeze-dried sediment using an Accelerated Solvent Extraction 350 with a CH_2Cl_2/MeOH (9:1 v/v) extraction solvent and four static cycles at 100°C. The total lipid extract was saponified using ~2 ml of a 0.5 M KOH in 95:5 MeOH:H_2O (optima grade). The neutral fraction, which contains the alkenones and the GDGTs, was obtained by extracting the saponification mixture using toluene. Silica gel column chromatography was used to separate the neutral fraction into a hydrocarbon fraction, a ketone fraction, and a polar fraction, respectively, eluted with 4 ml of Hexane, 4ml of CH_2CL_2, and 4ml of MeOH, allowing better subsequent analysis of compounds of interest.

The ketone fraction (eluted with 4 ml of CH_2Cl_2), containing the alkenones, was analyzed at ETH Zürich and the Lamont-Doherty Earth Observatory (Columbia University, USA). The ketone fraction was dried under an N_2 stream and dissolved in toluene and injected, for quantification. At ETHZ, samples were analyzed on a Thermo Scientific Trace 1310 Gas Chromatograph (GC) equipped with a non-polar (60 m × 0.25 mm × 0.25 μm) capillary column (ZB-1ms, Zebron™) with 5-m guard column and 2-ml/min He carrier gas flow. Sample was injected into a programmable temperature vaporization inlet, and the GC oven was ramped from 90 to 200°C at 40°C/min, 5°C/min to 300°C, and held 15 min to finally ramp 2°C/min to 320°C. At LDEO, samples were analyzed on a non-polar J&W DB-1 column with equivalent dimensions. GC oven was ramped from 90 to 250°C at 25°C/min, then ramped from 275 to 313 at 1°C/min and then 10°C/min to 320°C and held isothermal for 20 min. Samples were quantified on both instruments by flame ionization detection.

Distribution and abundance of the C_{37} diunsaturated and triunsaturated ketones were used to estimate the $U^{k'}_{37}$ ratio defined by (Brassell et al., 1986). A known amount of the C_{36} n-alkane (n-hexatriacontane; ETHZ) or stearyl stearate (LDEO) was added as an internal standard to the samples, and replicates were injected in every sequence for long-term validation and instrument drift which yielded a precision of 0.00063 $U^{k'}_{37}$ units. Intercomparing results from the same samples at ETHZ and LDEO demonstrated no systematic difference and excellent reproducibility between labs.

The polar fractions from a subset of 29 samples from Site U1406A, containing the GDGTs, were filtered through a 0.45-μm pore size and analyzed by high-performance liquid chromatography at ETH Zürich. An Agilent 1260 Series high-performance liquid chromatography equipped with Acquity BEH HILIC columns (150 mm × 2.1 mm × 1.7 μm) was used to calculate branched isoprenoid tetraether and TEX_{86} ratios (Kim et al., 2010). Instrument 1-sigma for TEX_{86} replicates was 0.0063 units.

Alkenone-derived SSTs were calculated from $U^{k'}_{37}$ using the BAYSPLINE calibration (Tierney & Tingley, 2018), a new reexamination of core top data, which incorporates a reduced temperature sensitivity and higher temperatures at high $U^{k'}_{37}$ ratios. Similarly, GDGT-derived SSTs were estimated applying the latest global Bayesian surface temperature spatial calibration (BAYSPARE) by Tierney & Tingley (2015). Previous published SSTs presented in the discussion were recalculated using the same calibrations.

2.3. Benthic Foraminifera

Bulk sediment samples that were previously freeze-dried and processed for organic extraction were sieved with deionized water through a 63-μm screen, ultrasonicated for 15-20 s to remove fine fraction, oven dried overnight at 50°C, and weighed. Our previous comparisons of stable isotopes in samples prior and after Accelerated Solvent Extraction extraction show no effect of solvents, consistent with negligible dissolution or reprecipitation in the intermediate polarity solvents used for extraction.

Benthic foraminifera were common, but not abundant, in all the samples, and are well preserved, with characteristic glassy surface in nearly all samples. In order to obtain deep water taxa, two certain deep sea-tracer species of benthic foraminifera were targeted (Coxall & Wilson, 2011; Lear et al., 2015): epifaunal C*ibicidoides* spp (mainly *C. mundulus*) and shallow infaunal *Oridorsalis umbonatus*.

Typically, we combined 5 to 10 benthic specimens larger than 200 μm, for each species. Foraminifera were crushed, rinsed two times with DI-water and once with methanol, then dried overnight at 50°C. Samples were analyzed at ETH Zurich on a GAS BENCH II system coupled to a Delta V Plus irMS (Thermo Scientific) following procedures described by Breitenbach and Bernasconi (2011) for small carbonate samples. Analytical precision for both stable isotopes is 0.07‰ after system calibration by two in-house standards and international carbonate standards NBS-19 and NBS-18. Values are reported relative to the Vienna PeeDee Belemnite standard. For 17 samples, replicate populations were picked and analyzed to evaluate the total reproducibility. Measurements yielded a mean replicate difference of 0.02‰ for δ^{13}C and 0.01‰ for δ^{18}O. Including replicate populations and multiple species, a total of 85 benthic isotope measurements are reported.

For an accurate isotopic record, the best strategy is to use a unique species for the entire interval. However, at some points, there were insufficient individuals of the species suggested to most closely reflect seawater isotopic values, the morphotypes *Cibicidoides* spp. (Katz et al., 2003). In these cases, *O. umbonatus* values were corrected to *Cibicidoides* spp. by applying the linear regression correction factor described by Beddow et al. (2016). On nine samples we were not able to find any of those targeted foraminifera. For 15 samples in which both *O. umbonatus* to *Cibicidoides* spp. were analyzed, the average difference after application of conversion from *O. umbonatus* to *Cibicidoides* spp. is 0.03‰ for δ^{18}O and 0.2‰ for δ^{13}C, which supports the sample δ^{18}O analysis derived from *O. umbonatus* exclusively. *Cibicidoides wullerstrorfi* was not analyzed when present because although it has no offset on δ^{18}O with the rest of *Cibicidoides* morphotypes, significant differences in δ^{13}C are reported at some stages (Gottschalk et al., 2016).

2.4. Coccolithophore Taxonomy

Slides were mounted for nannofossil assemblage analysis following the protocol described by Flores and Sierro (1997). A total of 40 randomly chosen field of views for each sample were imaged by a Zeiss Axiocam 506 Color camera coupled to a Zeiss Axio Scope HAL100 POL microscope configured with circular polarization. Individual nannofossil images were generated (an average of 700 for each sample) after processing the bulk images with MATLAB runtime software C-Calcita (Fuertes et al., 2014) and manually classified by taxonomy. Abundance of selected specimens was calculated as a percentage of all the coccoliths.

2.5. Grain Size Analysis

Sedimentological analysis of the lithogenic fraction from a subset of samples was carried out as in McCave et al. (1995). Lipid-extracted sediment was wet-sieved through 63-μm mesh to isolate the fine fraction. $CaCO_3$ was removed from 2 g of <63-μm fine fraction after slow digestion for 48 hr in 1M HCl. Decarbonated samples were rinsed afterward to a neutral pH. Biogenic opal was higher than 5% based upon smear slide evaluation, and thus, samples were processed to remove it by heating the sediment for 5 hr at 85°C in a 2M solution of Na_2CO_3. Following this step, any samples that still contained >5% biogenic silica in microscope slides were not measured for grain size. Finally, once washed and dispersed in polyphosphate solution for overnight rotation, samples were measured with a Malvern Hydro 2000S/G Diffraction Grain Sizer to obtain the grain size distribution. The mean Sortable Silt was calculated from the percentage of non-cohesive fine fraction (10 μm to 63 μm) that might be affected by the long-term resuspension (McCave, 2008; McCave et al., 1995).

3. Results

### 3.1. Calcareous Nannofossil Assemblages and Sortable Silt

Coccolithophore assemblage counts reveal pronounced variations in the relative abundance of the taxon *Helicosphaera* spp., with very low abundance in the early Oligocene, local maxima in abundance preceding and following the Oligocene-Miocene boundary (O/M boundary), and peak abundances of 10% by 18 Ma
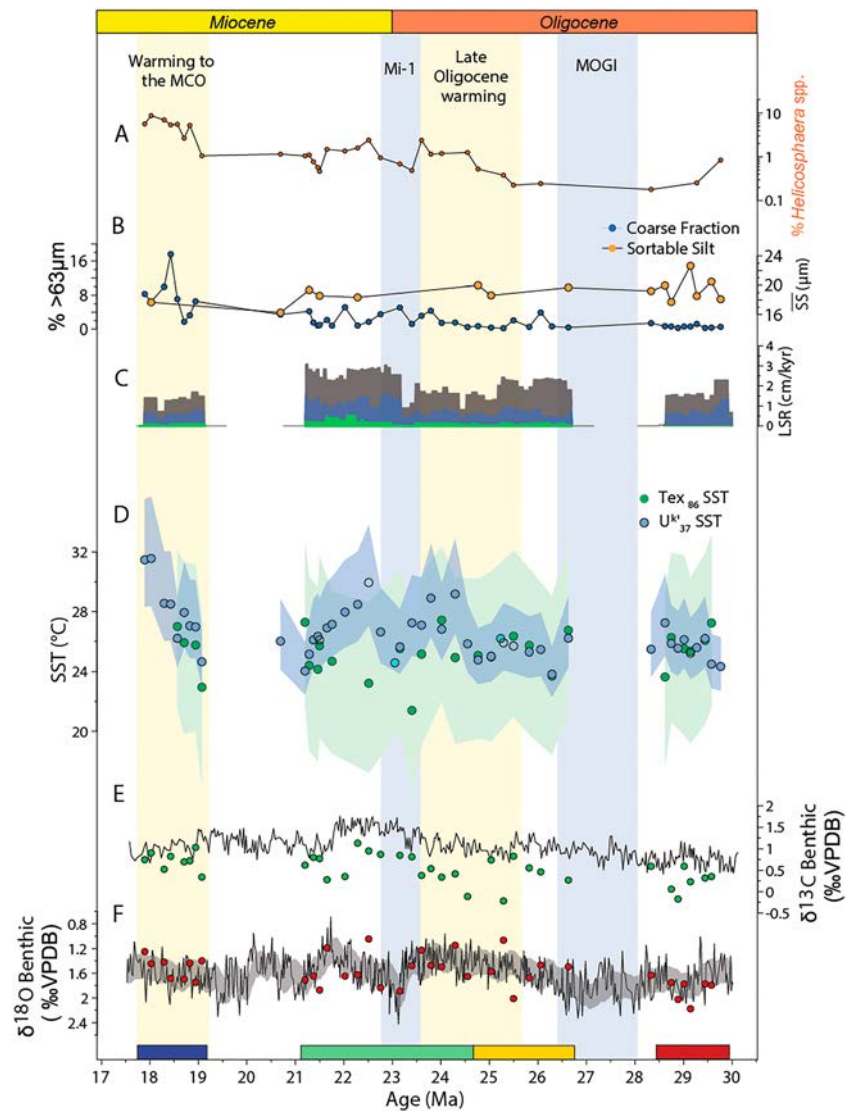
Figure 3. Sedimentological and geochemical indicators from Integrated Ocean Drilling Program 1406A. (a) Relative abundance of coccolith *Helicosphaera* spp. (b) Grain size: mean sortable silt in μm (orange dots) and percentage of coarse fraction (blue dots). (c) Site 1406A linear sedimentation rate (black), carbonate accumulation rate (blue), and radiolarian and diatom accumulation rate (green). (d) Sea surface temperatures (SSTs): Site 1406A TEX_{86} (green) and a $U^{k'}_{37}$ (blue, where empty circles indicate samples whose benthic $\delta^{18}O$ falls more than 0.2 ‰ from the moving average band from of the benthic megasplice De Vleeschouwer et al., 2017; and could reflect extremes in orbital cycle); alkenone SST from Site 1405A (turquoise). The blue and green bands correspond to 84th-16th and 95th-5th CIs for $U^{k'}_{37}$ BAYSPLINE and TEX_{86} BAYSPARE calibration, respectively. (e) $\delta^{13}C$ of benthic foraminifera from Site 1406A (green dots) overlapping Liebrand et al. (2016) data from Walvis Ridge Site 1264. (f) Site 1406A $\delta^{18}O$ benthic (red dots) over the megasplice $\delta^{18}O$ benthic compilation from De Vleeschouwer et al. (2017). Both compilations adjusted here to Geologic Time Scale 2012 (Gradstein et al., 2012). Color segments on *x* axis show distinct intervals plotted in Figure 4.

(Figure 3a). *Helicosphaera* spp. abundance is negatively correlated with *Noelaerhabdaceae* abundance, the most common family in the section.

The sortable silt grain size varies little over the studied interval (Figure 3b). Average values are 20 μm with a maximum of 22.6 μm at 29.1 Ma and minimum of 16.2 μm at 20.7 Ma. Percentages of coarse bulk fraction were always under 10% (average 3%) of whole dry sample for most of the samples. Linear sedimentation rate (LSR) and fraction of carbonate accumulation were calculated after the age model presented in this study
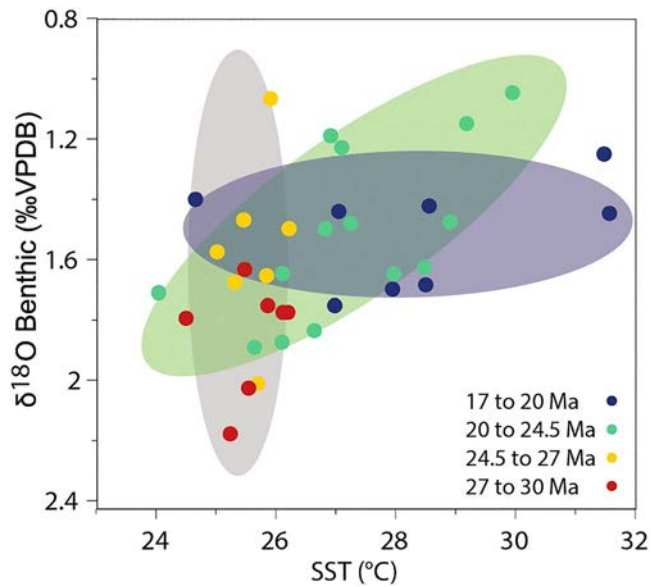
Figure 4. Correlation plot of alkenone sea surface temperature and $\delta^{18}O$ benthic foraminifera from Site 1406 with colors denoting specific time intervals. Data set r^2 values: 0.10 (17-20 Ma), 0.41 (20-24.5 Ma), and 0.04 (24.5-30 Ma).

(Figure 3c). Shipboard diatom and radiolarian relative abundance was used to construct the biogenic silica linear accumulation rates.

3.2. Sea Surface Temperatures

For the studied time interval 30 to 17.7 Ma, the $U_{37}^{k'}$-derived SSTs from Site 1406A indicate temperatures warmer than 23.8°C and maximum temperatures in excess of 30°C according to the BAYSPLINE calibration (Figure 3d). The two temperature determinations from the deeper site 1405A are consistent with coeval temperatures from Site 1406.

At Site 1406A, similar $U_{37}^{k'}$ temperature ranges, averaging 25°C, occur before the hiatus of the Mid-Oligocene Glacial Interval and during the 2 My after the hiatus. Temperatures warm rapidly in the Late Oligocene to reach 30°C by 24.4 Ma. The Oligocene-Miocene boundary and Mi-1 event is marked by a gradual two-step cooling in alkenone temperatures to a minimum of 25.6°C. Following the O/M boundary, temperature increases abruptly up to the calibration threshold followed by a decrease down to 24°C by 21.1 Ma, prior to the second hiatus. The last part of our record represents a warming leading up to the Middle Miocene Climatic Optimum, reaching the upper calibration limit after 18 Ma. No relationship is evident between alkenone concentration and SSTs for the studied interval (Fig. S1 and S2 in the supporting information).

GDGT-derived temperature estimates were produced only from a subset of the samples employed for alkenone measurements. Temperatures derived from the analysis of GDGTs have greater uncertainty due to both the wider uncertainty interval in calibration and uncertainty in the stability of the GDGT production depth. Nevertheless, with the exception of two points before and after the O/M boundary, TEX_{86} and $U_{37}^{k'}$ temperatures are comparable at all points in the record. However, branched isoprenoid tetraether index denotes moderate to high terrestrial input (Fig. S3), and in several cases, larger terrestrial input corresponds with samples for which TEX_{86} record differs markedly from the $U_{37}^{k'}$ temperatures. Specific trends are more difficult to compare due to the lower resolution of the TEX_{86} record compared to the $U_{37}^{k'}$ record.

3.3. Stable Isotopes in Benthic Foraminifera

The $\delta^{18}O$ values of benthic foraminifera range between 1.05‰ and 2.18‰ Vienna PeeDee Belemnite (Figure 3e). Although sampled at lower resolution, the temporal variations in benthic $\delta^{18}O$ from 1406A are consistent with long term trends in the benthic $\delta^{18}O$ megasplice (De Vleeschouwer et al., 2017), which in this time interval is comprised of data from IODP 1218, ODP 1090, ODP 926, and IODP 1337 (Figure 3e). The majority of 1406A benthic $\delta^{18}O$ fall within the envelope of the orbital scale variability in the megasplice. A $\pm0.2‰$ range around a 5-point mean moving window is used to highlight samples which fall far from the mean benthic $\delta^{18}O$ of the time window. SST estimation for these samples would correspond to periods of extremes in orbital cycles as expressed in benthic $\delta^{18}O$.

Paired alkenone SST and benthic $\delta^{18}O$ at 1406A show different degrees of correlation in different time slices (Figure 4). From 30 to 24.5 Ma, small variations in SST are not significantly correlated to the large 1.2‰ changes in benthic $\delta^{18}O$. In contrast, the interval from 24.5 to 22 Ma is characterized by significant correlation, with higher SST corresponding with more negative benthic $\delta^{18}O$ signal, and both showing large variations. In the early Miocene, after the SST recovery at 22.5 Ma, large variations in SST correspond to a smaller (0.7‰) range of $\delta^{18}O$, and the correlation is weak.

Benthic $\delta^{13}C$ varies by about 1‰ between 30 and 17 Ma and is on average lower than benthic $\delta^{13}C$ from the South Atlantic at Walvis Ridge (Liebrand et al., 2016) (Figure 3d). Although the 1406 record is of lower resolution, the offset from South Atlantic nonetheless is variable. No significant correlations exist between the benthic $\delta^{13}C$ and $\delta^{18}O$ (Fig. S4).

4. Discussion

4.1. Origin of SST Signal at IODP Site 1406

The surface ocean region potentially contributing particles to deep sea sediments has been described by a "statistical funnel" that is the result of both vertical and horizontal movement of particles in the ocean (Siegel & Deuser, 1997). Deeper depositional sites, and areas with stronger mean current velocities above the sediment, are expected to have a more extensive statistical funnel or surface "catchment area," as are more slowly settling particles. For example, off modern Bermuda, 90% of slowly sinking (50 m/day) particles settling to a depth of 3,200-m originate in a statistical funnel with a diameter of about 400 km (Siegel & Deuser, 1997). The explicit calculation of the dimensions of the statistical funnel requires knowledge of current speeds and directions throughout the overlying water column, information which is not available for the Oligocene to Early Miocene interval.

We suggest that the estimated SST trends reflect those in the region overlying Site 1406A. This interpretation is supported by several lines of evidence. First, the surface waters overlying Site 1406A show signs of relatively high biological productivity, for example, the continued deposition of diatoms and radiolaria throughout the studied interval (Norris et al., 2014). High productivity is typical of the modern continental margin setting. A high productivity in overlying waters provides a direct source of alkenones to the sediments, limiting the relative significance of alkenones that may be transported from the more distal regions of the statistical funnel. This situation contrasts with other depositional drift settings with oligotrophic conditions and limited productions of alkenones in the overlying waters, such as at Bermuda Rise, which may feature a substantial allochtonous alkenone population (Ohkouchi et al., 2002). Second, the delivery rate of the silt fraction, which effectively scavenges alkenones, excepting hiatuses, shows limited variations, and major SST fluctuation occurs in time intervals characterized by constant silt delivery rate. Mean sortable silt and coarse fraction percentage, indicators of deep circulation, show limited variation (Figure 3b) for this million-year timescale framework and do not correlate with SST variation. There is therefore no evidence that cycles in SST could be artifacts of variations in the origin of alkenones due to changing depositional dynamics.

Today, phytoplankton production in the Northern Atlantic is enhanced during spring bloom due to the reduction in the mixed layer depth and increased light (Behrenfeld et al., 2005). This production dynamic may not be representative for the Oligocene, because a poleward expansion of the subtropical gyre under warmer climates could also entail a poleward shift in the limit of deep winter mixing leading to a spring bloom. Regardless, the seasonality of phytoplankton production is strongly attenuated in alkenone export because higher alkenone flux correlates with a higher rate of degradation rate during sinking, leading to negligible seasonal bias in alkenone SST even in sites with strongly seasonal production (Rosell-Melé & Prahl, 2013). Consequently, we have little reason to believe that there would have been a strong seasonal bias to the temperature signal recorded the 1406A in the Oligocene, and rather we suggest, as today, it reflects an annual SST.

Site 1406A is the shallowest site (3,800 m bsl) of Leg 342 and possesses the most pelagic-dominated sediment source due to its position above most of the core path of the Deep Western Boundary Current, and the accumulation rates are consistent with limited long-term change in the sediment depositional regime. The similarity in absolute temperatures between Site 1406A and 1405A, during times when the temporal correlation of these sites is precise, suggests that at least at these time periods, there was no significant difference in the SST for the catchment area at approximately 3,800- and 4,300-m depths.

During some time intervals, the 1406A temperature estimates differ in absolute values and trends from those of the proximal but deeper Site 1404 (Liu et al., 2018; modern location: 40.00°N, 51.60°W; 4, 710 m bsl; Figure 1). Temperatures are compared here for both records using the BAYSPLINE calibration (Tierney & Tingley, 2018). Trends from the two sites diverge between 29.5 to 28.4 Ma, when the Site 1404 record suggests a 4°C decline in temperatures, but Site 1406A shows constant and warmer temperatures around ~26°C (Figure 5a). Trends also diverge just above the Miocene/Oligocene boundary, when cold temperatures persist longer in Site 1404, through 22.49 Ma, leading to a 5° temperature difference relative to Site 1406A. Subsequently, Site 1404 temperatures rise until 20 Ma, while Site 1406A temperatures are cooling.
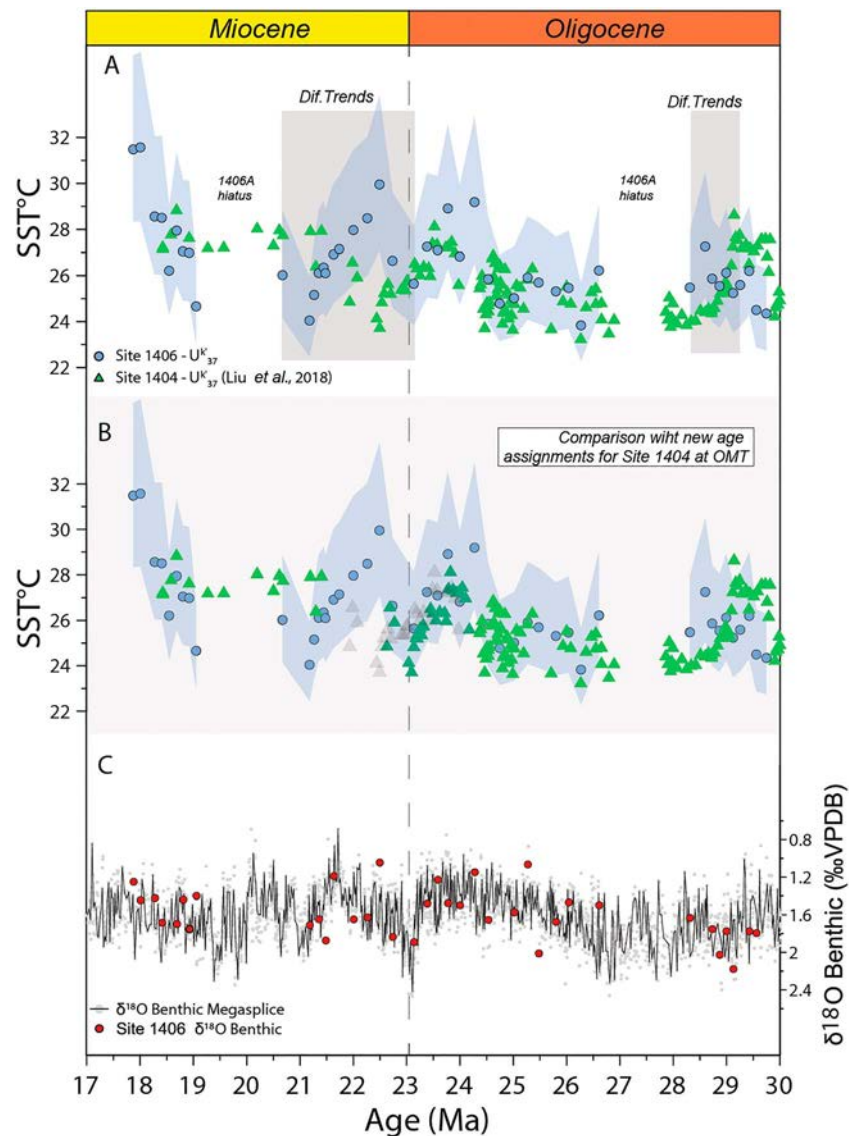
Figure 5. Comparison of $U^{k'}_{37}$ new 1406A sea surface temperatures trends and published from Site 1404. (a) Original data updated to the same calibration (BAYSPLINE) and age timescale (Geologic Time Scale 2012). (b) Sea surface temperature (SST) record with proposed new age assignments (dark green) for Site 1404 around the O/M boundary. Original data are shown with transparent triangles. (c) Benthic $\delta^{18}O$ on Site 1406A and megasplice compilation from De Vleeschouwer et al. (2017).

Several factors may contribute to discrepancies between the Site 1406A and Site 1404 records. Importantly, we find no significant difference in alkenone temperatures between 4300 (1405A) and 3800 (1406A) m water depth, when the age correlation is precise. It is possible that the depositional environment at the deeper Site 1404 is more dynamic than at the shallower 1406A, which could both contribute to greater chronological uncertainties and potentially cause variation in alkenone source area. Site 1404 has a greater temporal variation and extremes in LSR (Fig. S5) than Site 1406A (Norris et al., 2014), potentially caused by greater sensitivity to current speed or depth. For instance, the divergence in temperature trends just after the O/M boundary is contemporary with an increase in LSR at 1404.

Uncertainties on the order of ~1 Myr in the age model at one or both sites could also lead to erroneous correlation, and this is our favored interpretation based on currently available data. The first discrepancy between sites occurs between 29.5 to 28.4 Ma when the age model for both sites is based on low

resolution shipboard biostratigraphy and magnetostratigraphy. During the second interval of divergence, between 22.7 to 21 Ma, the age model for 1406A is based on higher resolution biostratigraphy and updated magnetostratigraphy and suggests stable LSR; our confidence in this Site 1406A age model is enhanced by the similar long-term trend in 1406A benthic $\delta^{18}O$ and megasplice $\delta^{18}O$. In contrast, at Site 1404 there is an abrupt change in LSR at 22.5 Ma and orbitally resolved benthic stratigraphy is not yet available. To test whether divergent age models could be responsible for the apparently contrasting trends, over the interval from 22.7 to 21 Ma, we adjusted the published age assignments uniquely from Site 1404 SST determinations to match trends in 1406A (Figure 5b). By shifting Site 1404 sample ages by 700 to 200kyr, consistent trends are recovered and both sites show a pronounced cold excursion with minimum at the Oligocene-Miocene boundary. The new age assignments are well within the uncertainty of the available 1404 age tiepoints (Fig. S6). Benthic foraminifera stable isotope data from Site 1404 paired to the SST depths could provide confirmation of this potential revision of chronology.

4.2. Surface Temperature Evolution on Newfoundland Bank and Relation to Benthic $\delta^{18}O$ and Antarctic Ice Sheet Variability

The new SST record generated here for Site 1406A confirms that very warm waters, typical of today's tropical latitudes, extended through midlatitudes in the western North Atlantic during the Oligocene to early Miocene, as suggested by previous biomarker studies (Liu et al., 2018; Super et al., 2018) as well as evidenced by Northern Hemisphere fossil flora records (Kotthoff et al., 2014; Larsson et al., 2006). Furthermore, our new data from both TEX_{86} and $U_{37}^{k'}$ at the same site confirm similar temperature estimates. Our higher resolution $U_{37}^{k'}$ record provides more precise temperature estimates and better resolution of temporal trends than the TEX_{86} at our site; because of these features, we use alkenone-derived temperatures for our further interpretations. Temperatures at 17.8 Ma reach the calibration limit of $U_{37}^{k'}$ BAYSPLINE; these samples contain a higher abundance of tropical nannofossils than the temperature maxima immediately preceding and following the Mi-1, which may indicate that temperatures were warmer at Site 1406A by 17.8 Ma than they were at any time in the preceding 12 Ma. The trends in $U_{37}^{k'}$ temperatures parallel closely the relative abundance of subtropical *Helicosphaera* spp., providing added confidence in the inferred temperature trends.

Our record reveals that long-term cycles in SST in the North-Atlantic midlatitudes, which although sampled at lower resolution than the prevailing obliquity and short eccentricity cycles in $\delta^{18}O$ (De Vleeschouwer et al., 2017; Liebrand et al., 2016), are not artifacts of variable sampling of orbital $\delta^{18}O$ extremes. The benthic $\delta^{18}O$ of nearly all of our analyzed SST points fall within 0.2‰ of the long-term running mean in the global benthic foraminifer megasplice (De Vleeschouwer et al., 2017; Figure 3e). Only the warmth at 22.49 Ma may be sampling an extreme in orbital cycle (see Figure 3c) and potentially amplifying the temperature maximum post-Mi-1; however, a similar extreme benthic $\delta^{18}O$ at 25.27 Ma does not yield temperatures significantly different from neighboring samples with benthic $\delta^{18}O$ well within the long-term mean. Therefore, we infer that our $U_{37}^{k'}$ record defines significant changes in mean temperature taking place at the north midlatitude to high latitude of the Atlantic Ocean.

North Atlantic average SST variations over broad intervals correlate with changes in the sensitivity of climate to obliquity forcing and to changes in the extent of the Antarctic ice sheet (Figure 6). The cool average temperatures characterizing the period from 30 to 24.5 Ma coincide with a period in which the Ross Sea sedimentation, proximal to the Antarctic Ice Sheet, was dominated by massive and stratified diamictite, with multiple major erosional hiatuses (Barrett et al., 2007). These ice-proximal records suggest that the ice sheet was principally extending into the marine realm during this interval and was at some points marine-grounded. Benthic $\delta^{18}O$ records have low sensitivity to obliquity forcing during this time interval (Levy et al., 2019). Subsequently, the warmer average North Atlantic temperatures between 24.5 and 21 Ma correspond with Ross Sea sedimentation dominated by nonglacially deposited sandstones and mudstones, interpreted as period when the ice sheet was predominantly land-based. The dramatic warming in the uppermost section of at Site 1406A appears to reflect warming leading up to the Middle Miocene Climatic Optimum. Given the high uncertainty in the Site 1406A age model at this interval (900kyr at 19 Ma decreasing to less than 100kyr at 18 Ma), it is possible that the warming is slightly younger than estimated here. If the Site 1406A age model overestimates age by 0.5 to 1 Myr, then it would coincide with the onset of the retreat of the marine-grounded ice sheet to terrestrial ice in the Ross Sea region

(Levy et al., 2016), and a return to high sensitivity of benthic δ^{18}O to obliquity at ~18 Ma. Over the longest continuous portion of our record with the best age control (26.5 to 20.5), minima in surface ocean temperature occur every ~2 Myr, which is in the range of long modulation of obliquity. In general, there is high sensitivity to obliquity in this interval.

Our comparison of Site 1406A benthic δ^{18}O and SST suggests a complex and temporally varying relationship between midlatitude SST and high-latitude temperature and ice volume. Site 1406A is suggested to be bathed in Northern Component Water by the latest Eocene (Coxall et al., 2018). During the generally cooler early- and mid-Oligocene intervals sampled, from 30 to 28 Ma and 26 until 24.5 Ma, variations in midlatitude SST are small (~1°C), yet our samples encompass a 0.8‰ range in benthic δ^{18}O (with a single sample extending range to 1.2‰) during a period when marine ice advance in the Ross sea sector was common (Figure 4). A large variation in benthic δ^{18}O, in the absence of appreciable midlatitude SST change, could reflect appreciable (>3-fold) polar amplification of SST change in deep-water formation areas if ice volume were constant, and/or ice volume as a significant component of benthic δ^{18}O. This period is marked by low sensitivity of megasplice benthic δ^{18}O to obliquity forcing (Figure 6b), which is interpreted to reflect a state when ice sheets responded to direct insolation forcing rather than regional temperature (Levy et al., 2019). At the same time, the amplitude of benthic δ^{18}O on short eccentricity timescale was also low (Liebrand et al., 2017). Although few comparisons exist of surface temperature and benthic δ^{18}O, long-term comparisons of deep ocean temperature and deep ocean δ^{18}O$_{sw}$ reveal periods of decoupling, which may reflect ice growth, which is most sensitive to temperature around key thresholds (Lear et al., 2015).

The sampled intervals around the O/M boundary and the rise to the Middle Miocene Climatic Optimum (MMCO) 17-14.5 Ma (Zachos et al., 2001) both reflect warmer average temperatures at Site 1406A, but these two warm intervals show two different relationships between benthic δ^{18}O and Site 1406A SST. In the ~1 Myr prior to and following the O/M boundary (from 24.5 to 22 Ma)—an interval encompassing both warmer temperatures and lower average benthic δ^{18}O than the preceding Oligocene—the larger amplitude (5°C) variation in midlatitude SST is coupled to a 1‰ range in benthic δ^{18}O, with the warmest temperatures coinciding with minima in benthic δ^{18}O. The Oligocene Miocene transition itself is marked by a two-step decrease in North Atlantic SST, analogous to the two-step rise in high resolution benthic δ^{18}O in orbitally resolved records (Liebrand et al., 2016; Mawbey & Lear, 2013), the pacing of which has been recently suggested to be driven by both changes in atmospheric carbon dioxide and obliquity (Greenop et al., 2019; Levy et al., 2019). Across the O/M boundary, previous high-resolution analysis of a tropical Atlantic site between 22.4 to 23.7 Ma showed that intervals of increased δ^{18}O$_{sw}$ interpreted as recording ice growth were coupled to intervals of bottom water cooling, inferred from benthic foraminiferal Mg/Ca (Mawbey & Lear, 2013). If bottom water temperature and ice volume components covary similarly in the preceeding ~1 Myr and subsequent ~0.4 Myr (i.e., between 24.5 and 22 Ma), then the significant covariation between midlatitude SST and benthic δ^{18}O in our record could reflect persistent coupling of midlatitude SST, high-latitude deepwater formation regions SSTs, and ice volume on orbital scale around the O/M boundary. During the Late Oligocene warming, ice-proximal sediments are deposited episodically in the Ross Sea, suggesting a dynamic response of the west Antarctic ice sheet (Barrett et al., 2007). It remains to be evaluated, whether this dynamic ice-margin response represents a significant ice volume fluctuation that would be appreciable in benthic δ^{18}O, or a state of high ice margin sensitivity but minimal total ice variation, in which temperature is a dominant component in benthic δ^{18}O. This entire interval is marked by high sensitivity of benthic δ^{18}O to obliquity forcing, and moderate to high amplitude of δ^{18}O variation at short eccentricity timescale.

The early Miocene warming we sample between ~19 and 17 Ma, leading up to MMCO, is also warmer than our early and middle Oligocene time intervals but features a different benthic δ^{18}O relationship than the O/M boundary (Figure 4). This period encompasses a >5°C temperature rise, which reaches the calibration limit of $U^{k'}_{37}$ BAYSPLINE and may underestimate the full temperature rise. Our samples encompass a limited, 0.4‰ range in benthic δ^{18}O across this warming trend, which is not significantly correlated with Site 1406A SST. One explanation for the lack of correlation is that this phase of warming was accompanied by minimal variation in ice volume and that SSTs in deep-water formation regions were less variable than SSTs at midlatitudes. Data on bottom water temperatures are sparse over this interval, but over the warming leading to peak MCO temperatures (17.5-15.4 Ma), the most reliable bottom water temperatures, estimated
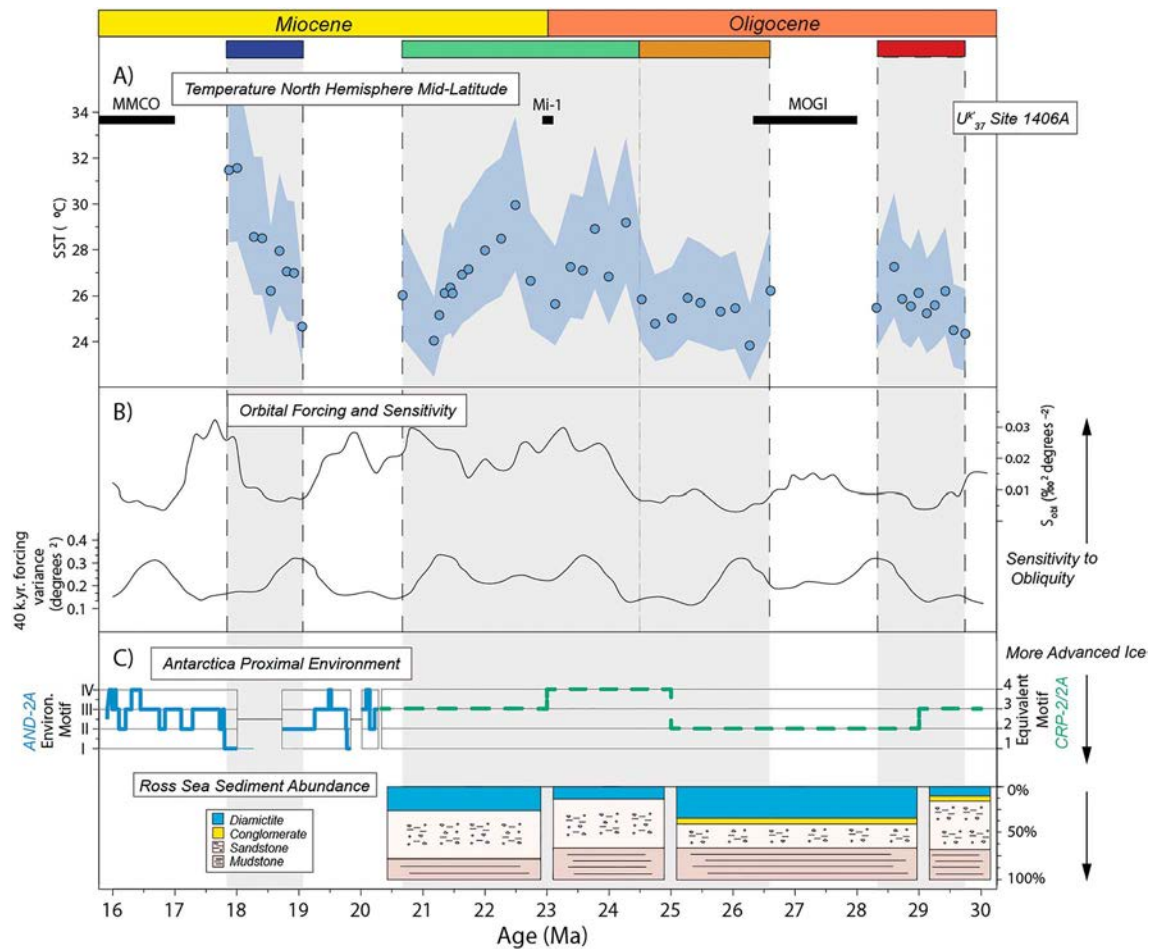
Figure 6. (a) Sea surface temperature from Site 1406A and its 16th and 84th confidence intervals. (b) Obliquity sensitivity (Levy et al., 2019) from obliquity forcing variance of benthic δ^{18}O. (c) The blue line shows Antarctic proximal environmental motifs from Levy et al. (2016) for the middle Miocene from ANDRILL cores; the black lines show disconformities. The dashed green line indicates variation in mean environmental settings according to lithofacies analysis from Cape Roberts Project drillcore CRP-2/2A (Barrett et al., 2007). The vertical bars show, for each of four intervals, illustrates the percentage of ice-derived sediments in CRP2/2A. The Cape Roberts Drill core also features major disconformities, but unlike ANDRILL, the CRP sequence lacks precise chronology for lithofacies boundaries. Color segments and grey shading area correspond to distinct intervals identified in the 1406A alkenone SST and δ^{18}O benthic foraminifera relationship plotted in Figure 4.

from infaunal benthic Mg/Ca at ODP Site 806, are not correlated benthic δ^{18}O (Lear et al., 2015). This suggests that not only midlatitude SST but also SST in high-latitude deepwater formation regions may be decoupled from ice volume components during this time.

Benthic foraminfera δ^{13}C values denote an interesting Atlantic circulation feature of lower values in this northern site than in the southern Walvis Ridge (Site 1264; Figure 3e). This trend has been also demonstrated through the Eocene (Coxall et al., 2018; Cramer et al., 2009), and our data show that it continues through the Oligocene.

4.3. Oligocene-Miocene Latitudinal Temperature Gradients in the North Atlantic

A comparison of our new Site 1406A temperature record with other published temperatures from the North Atlantic shows a distinct lack of latitudinal temperature gradient (Figure 7). TEX$_{86}$ temperatures from equatorial Site 925 (Zhang et al., 2013) are within the same range of those from subtropical Sites 1406A and DSDP Site 608 (Super et al., 2018; modern coordinates: 42°50.205′N, 23°05.250′W) in the Oligocene and early Miocene. Such gradient has been reduced back in the early Oligocene (Zhang et al., 2019). However, the interval pre-O/M boundary appears to have a reduced (2°C) offset between midlatitude and equatorial locations. The reconstructed gradient could be underestimated if GDGT production depths in
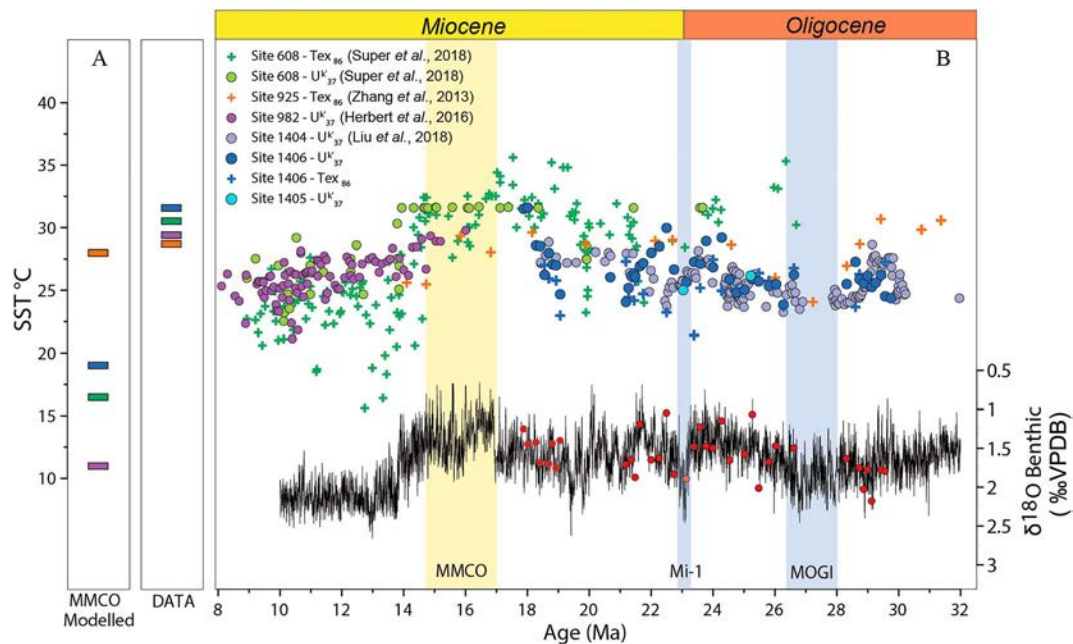
Figure 7. North Atlantic Oligocene Miocene temperature records. Site locations on Figure 1. (a) For four different locations in the North Atlantic, comparison of annual average sea surface temperature (SST) modeled by the CCSM3 model for the Middle Miocene Climatic Optimum assuming Miocene paleogeography and 400 ppmv CO_2 by Frigola et al. (2018) and average SST proxy data for the broad MCO interval from 18 to 14.5 Ma. The color of each bar matches the color of the symbol for proxy locations whose SST is shown in the compilation of (b) Ocean Drilling Program (ODP) 925 (4°N, 43°W; orange); Integrated Ocean Drilling Program (IODP) 1406 (40N, 50°W; blue); ODP 608 (42°N, 23°W;green); ODP 982 (58°N, 16°W; purple). (b) $U^{k'}_{37}$ temperatures after BAYSPLINE calibration (filled circles) and GDGT-derived BAYSPARE (empty circles). Bottom plot on panel b shows benthic foraminiferal $\delta^{18}O$ from deVleeschower et al. (2017) and Site 1406 new data. Vertical band denotes main cold and warm intervals defined by Zachos et al. (2001) and Liebrand et al. (2017). All plotted ages against Gradstein et al. (2012) timescale.

the equatorial site were deeper than those at Site 1406A and 1404, therefore selectively underestimating temperatures at the tropical sea surface.

On the other hand, the data suggest an apparent longitudinal gradient in temperature. Reported SST from the Eastern Atlantic at Site 608 are derived primarily from GDGTs; excluding cold Mi-1a and Mi-1 events, temperatures are above 30°C with intervals during the MMCO up to 35°C, significantly warmer than GDGT temperatures at Site 1406. Yet, of the four alkenone temperature estimations at Site 608 during our studied interval, two yield similar temperatures and two yield much warmer temperatures than Site 1406. From alkenone SST, it is difficult to evaluate the longitudinal temperature gradient with this limited information. Given the uncertainty in the consistency of GDGT production depth among the sites, it may be premature to conclude from the GDGT temperature comparison that the Oligocene-Miocene featured a strong heat transport from west to east as has been suggested for the middle Miocene (Utescher et al., 2017). Clear evidence for significant northward heat transport emerges at the end of the MMCO, even as far north as 50°N latitude in the eastern Atlantic Site 982, alkenone record temperatures in excess of 30°C (recalculated from (Herbert et al., 2016) using the BAYSPLINE calibration).

Paleoclimate model simulations with relevant paleogeography for the MMCO and 400 ppmv CO_2 do not reproduce the extremely warm temperatures in the extra-tropical North Atlantic sites, and simulate a much stronger latitudinal gradient between the equatorial site and the locations of extratropical records (Frigola et al., 2018; Herold et al., 2012). Simulations of Paleocene Eocene Thermal Maximum, which feature different paleogeography, using 2250 ppmv CO_2 and altered cloud feedbacks, simulate extreme midlatitude temperatures of 30°C at 42°N in the western Atlantic. However, these simulations maintain a latitudinal SST gradient of ~8°C between the locations of Sites 925 and 1406 (Kiehl & Shields, 2013), still much lower than inferred from the Oligocene TEX_{86} temperatures, although temperatures could be underestimated at these equatorial location due to uncertainties in the TEX_{86} proxy. Our observations are consistent with a recent a data-model comparison for the Eocene (Evans et al., 2018) and highlight the difficulty of simulating the

absolute temperature and latitudinal temperature gradients of warm earth climates, including the Eocene and early Miocene as shown here.

5. Conclusions

New SST reconstructions at IODP Site 1406A offshore Newfoundland confirm that tropical SSTs reached as far as midlatitude to high latitude from the late Oligocene to early Miocene. Average conditions were colder in the early and middle Oligocene prior to 24.5 Ma, followed by warmer average climate, reaching peak temperatures in the youngest part of the record leading in to the mid-Miocene. Our records indicate significant million-year-scale variations in temperature throughout the Oligocene and early Miocene. The Oligocene-Miocene transition is marked by a two-step cooling, but the oscillations in temperature in the best-dated portion of our record appear to follow an ~2-Myr cyclicity, in which the Oligocene-Miocene transition temperature minimum is potentially paced by long obliquity cycles. Paired benthic δ^{18}O and SST show contrasting relationships in different time intervals: the early- and mid-Oligocene was characterized by an unstable but cooler Antarctic, while the warmer Oligocene-Miocene transition featured strong SST and benthic δ^{18}O covariance. Leading into the Middle Miocene Climatic Optimum, we observe a pronounced warming of the midlatitude North Atlantic without significant correlated change in benthic δ^{18}O, suggesting minimal variation in ice volume and deep-water formation SSTs less variable. Our new data support previous findings from the northern hemisphere, which characterized a warm midlatitude ocean. These temperature patterns have not modeled yet for this time period, possible suggesting currently unidentified feedbacks in the climate system. We also highlight the strongly reduced latitudinal temperature gradients during the warmer Oligocene and early Miocene climates.

References

Barrett, P., Hambrey, M., Christoffersen, P., Glasser, N., & Hubbart, B. (2007). Cenozoic climate and sea level history from glacimarine strata off the Victoria Land coast, Cape Roberts Project, Antarctica. In M. J. Hambrey, P. Christoffersen, N. F. Glasser, & B. Hubbart (Eds.), *Glacial sedimentary processes and products*, *International Association of Sedimentologists*, (Vol. 39, pp. 259–287).

Beddow, H. M., Liebrand, D., Sluijs, A., Wade, B. S., & Lourens, L. J. (2016). Global change across the Oligocene-Miocene transition: High-resolution stable isotope records from IODP Site U1334 (equatorial Pacific Ocean). *Paleoceanography*, *31*, 81–97. https://doi.org/10.1002/2015PA002820

Behrenfeld, M. J., Boss, E., Siegel, D. A., & Shea, D. M. (2005). Carbon-based ocean productivity and phytoplankton physiology from space. *Global biogeochemical cycles*, *19*, GB1006. https://doi.org/10.1029/2004GB002299

Blaauw, M., & Christen, J. A. (2011). Flexible paleoclimate age-depth models using an autoregressive gamma process. *Bayesian analysis*, *6*, 457–474.

Boyle, P. R., Romans, B. W., Tucholke, B. E., Norris, R. D., Swift, S. A., & Sexton, P. F. (2017). Cenozoic North Atlantic deep circulation history recorded in contourite drifts, offshore Newfoundland, Canada. *Marine Geology*, *385*, 185–203. https://doi.org/10.1016/j.margeo.2016.12.014

Bralower, T. J. (2002). Evidence of surface water oligotrophy during the Paleocene-Eocene thermal maximum: Nannofossil assemblage data from Ocean Drilling Program Site 690, Maud Rise, Weddell Sea. *Paleoceanography*, *17*(2), 1023. https://doi.org/10.1029/2001PA000662

Brassell, S., Eglinton, G., Marlowe, I., Pflaumann, U., & Sarnthein, M. (1986). Molecular stratigraphy: a new tool for climatic assessment. *Nature*, *320*(6058), 129–133. https://doi.org/10.1038/320129a0

Breitenbach, S. F., & Bernasconi, S. M. (2011). Carbon and oxygen isotope analysis of small carbonate samples (20 to 100 μg) with a GasBench II preparation device. *Rapid Communications in Mass Spectrometry*, *25*(13), 1910–1914. https://doi.org/10.1002/rcm.5052

Coxall, H. K., Huck, C. E., Huber, M., Lear, C. H., Legarda-Lisarri, A., O'regan, M., et al. (2018). Export of nutrient rich Northern Component Water preceded early Oligocene Antarctic glaciation. *Nature Geoscience*, *11*(3), 190–196. https://doi.org/10.1038/s41561-018-0069-9

Coxall, H. K., & Wilson, P. A. (2011). Early Oligocene glaciation and productivity in the eastern equatorial Pacific: Insights into global carbon cycling. *Paleoceanography and Paleoclimatology*, *26*, PA2221. https://doi.org/10.1029/2010PA002021

Cramer, B., Toggweiler, J., Wright, J., Katz, M., & Miller, K. (2009). Ocean overturning since the Late Cretaceous: Inferences from a new benthic foraminiferal isotope compilation. *Paleoceanography and Paleoclimatology*, *24*, PA4216. https://doi.org/10.1029/2008PA001683

De Vleeschouwer, D., Vahlenkamp, M., Crucifix, M., & Pälike, H. (2017). Alternating Southern and Northern Hemisphere climate response to astronomical forcing during the past 35 my. *Geology*, *45*(4), 375–378. https://doi.org/10.1130/G38663.1

Deconto, R. M., Pollard, D., Wilson, P. A., Palike, H., Lear, C. H., & Pagani, M. (2008). Thresholds for Cenozoic bipolar glaciation. *Nature*, *455*, 652–656. https://doi.org/10.1038/nature07337

Evans, D., Sagoo, N., Renema, W., Cotton, L. J., Müller, W., Todd, J. A., et al. (2018). Eocene greenhouse climate revealed by coupled clumped isotope-Mg/Ca thermometry. *Proceedings of the National Academy of Sciences*, *115*(6), 1174–1179. https://doi.org/10.1073/pnas.1714744115

Faugères, J.-C., Stow, D. A., Imbert, P., & Viana, A. (1999). Seismic features diagnostic of contourite drifts. *Marine Geology*, *162*(1), 1–38. https://doi.org/10.1016/S0025-3227(99)00068-7

Flores, J., & Sierro, F. (1997). Revised technique for calculation of calcareous nannofossil accumulation rates. *Micropaleontology*, *43*(3), 321–324. https://doi.org/10.2307/1485832

Frigola, A., Prange, M., & Schulz, M. (2018). Boundary conditions for the Middle Miocene Climate Transition (MMCT v1. 0). *Geoscientific Model Development*, *11*(4), 1607–1626. https://doi.org/10.5194/gmd-11-1607-2018

Fuertes, M.-Á., Flores, J.-A., & Sierro, F. J. (2014). The use of circularly polarized light for biometry, identification and estimation of mass of coccoliths. *Marine Micropaleontology*, *113*, 44–55. https://doi.org/10.1016/j.marmicro.2014.08.007

Gallagher, S. J., Villa, G., Drysdale, R. N., Wade, B. S., Scher, H., Li, Q., et al. (2013). A near-field sea level record of East Antarctic Ice Sheet instability from 32 to 27 Myr. *Paleoceanography*, *28*, 1–13. https://doi.org/10.1029/2012PA002326

Gard, G., & Backman, J. (1990). Synthesis of Arctic and Sub-Arctic coccolith biochronology and history of North Atlantic drift water influx during the last 500.000 years. In *Geological history of the polar oceans: Arctic versus Antarctic*, (pp. 417–436). Dordrecht: Springer.

Gasson, E., DeConto, R. M., Pollard, D., & Levy, R. H. (2016). Dynamic Antarctic ice sheet during the early to mid-Miocene. *Proc Natl Acad Sci U S A*, *113*, 3459–3464. https://doi.org/10.1073/pnas.1516130113

Gottschalk, J., Vázquez Riveiros, N., Waelbroeck, C., Skinner, L. C., Michel, E., Duplessy, J.-C., et al. (2016). Carbon isotope offsets between benthic foraminifer species of the genus Cibicides (Cibicidoides) in the glacial sub-Antarctic Atlantic. *Paleoceanography*, *31*, 1583–1602. https://doi.org/10.1002/2016PA003029

Gradstein, F. M., Ogg, J. G., Schmitz, M., & Ogg, G. (2012). *The geologic time scale 2012*. Amsterdam, The Netherlands: Elsevier.

Greenop, R., Sosdian, S. M., Henehan, M. J., Wilson, P. A., Lear, C. H., & Foster, G. L. (2019). Orbital forcing, ice-volume and CO_2 across the Oligocene-Miocene Transition. *Paleoceanography and Paleoclimatology*, *34*, 316–328. https://doi.org/10.1029/2018PA003420

Hall, M. M., Torres, D. J., & Yashayaev, I. (2013). Absolute velocity along the AR7W section in the Labrador Sea. *Deep Sea Research Part I: Oceanographic Research Papers*, *72*, 72–87. https://doi.org/10.1016/j.dsr.2012.11.005

Herbert, T. D., Lawrence, K. T., Tzanova, A., Peterson, L. C., Caballero-Gill, R., & Kelly, C. S. (2016). Late Miocene global cooling and the rise of modern ecosystems. *Nature Geoscience*, *9*(11), 843–847. https://doi.org/10.1038/ngeo2813

Herold, N., Huber, M., Müller, R., & Seton, M. (2012). Modeling the Miocene climatic optimum: Ocean circulation. *Paleoceanography and Paleoclimatology*, *27*, PA1209. https://doi.org/10.1029/2010PA002041

Ho, S. L., & Laepple, T. (2016). Flat meridional temperature gradient in the early Eocene in the subsurface rather than surface ocean. *Nature Geoscience*, *9*(8), 606–610. https://doi.org/10.1038/ngeo2763

Hohbein, M. W., Sexton, P. F., & Cartwright, J. A. (2012). Onset of North Atlantic Deep Water production coincident with inception of the Cenozoic global cooling trend. *Geology*, *40*(3), 255–258. https://doi.org/10.1130/G32461.1

Hurley, S. J., Lipp, J. S., Close, H. G., Hinrichs, K.-U., & Pearson, A. (2018). Distribution and export of isoprenoid tetraether lipids in suspended particulate matter from the water column of the Western Atlantic Ocean. *Organic geochemistry*, *116*, 90–102. https://doi.org/10.1016/j.orggeochem.2017.11.010

Katz, M. E., Katz, D. R., Wright, J. D., Miller, K. G., Pak, D. K., Shackleton, N. J., & Thomas, E. (2003). Early Cenozoic benthic foraminiferal isotopes: Species reliability and interspecies correction factors. *Paleoceanography*, *18*(2), 1024. https://doi.org/10.1029/2002PA000798

Kiehl, J. T., & Shields, C. A. (2013). Sensitivity of the Palaeocene-Eocene Thermal Maximum climate to cloud properties. *Philos Trans A Math Phys Eng Sci*, *371*. https://doi.org/10.1098/rsta.2013.0093

Kim, J.-H., Van der Meer, J., Schouten, S., Helmke, P., Willmott, V., Sangiorgi, F., et al. (2010). New indices and calibrations derived from the distribution of crenarchaeal isoprenoid tetraether lipids: Implications for past sea surface temperature reconstructions. *Geochimica et Cosmochimica Acta*, *74*(16), 4639–4654. https://doi.org/10.1016/j.gca.2010.05.027

Kotthoff, U., Greenwood, D., McCarthy, F., Müller-Navarra, K., Prader, S., & Hesselbo, S. (2014). Late Eocene to middle Miocene (33 to 13 million years ago) vegetation and climate development on the North American Atlantic Coastal Plain (IODP Expedition 313, Site M0027). *Clim. Past*, *10*(4), 1523–1539. https://doi.org/10.5194/cp-10-1523-2014

Larsson, L. M., Vajda, V., & Rasmussen, E. S. (2006). Early Miocene pollen and spores from western Jylland, Denmark-environmental and climatic implications. *GFF*, *128*(3), 261–272. https://doi.org/10.1080/11035890601283261

Lear, C. H., Coxall, H. K., Foster, G. L., Lunt, D. J., Mawbey, E. M., Rosenthal, Y., et al. (2015). Neogene ice volume and ocean temperatures: Insights from infaunal foraminiferal Mg/Ca paleothermometry. *Paleoceanography*, *30*, 1437–1454. https://doi.org/10.1002/2015PA002833

Levy, R., Harwood, D., Florindo, F., Sangiorgi, F., Tripati, R., von Eynatten, H., et al. (2016). Antarctic ice sheet sensitivity to atmospheric CO2 variations in the early to mid-Miocene. *Proc Natl Acad Sci U S A*, *113*, 3453–3458. https://doi.org/10.1073/pnas.1516030113

Levy, R., Meyers, S., Naish, T., Golledge, N., McKay, R., Crampton, J., et al. (2019). Antarctic ice-sheet sensitivity to obliquity forcing enhanced through ocean connections. *Nature Geoscience*, *12*, 132–137.

Liebrand, D., Beddow, H. M., Lourens, L. J., Pälike, H., Raffi, I., Bohaty, S. M., et al. (2016). Cyclostratigraphy and eccentricity tuning of the early Oligocene through early Miocene (30.1–17.1 Ma): Cibicides mundulus stable oxygen and carbon isotope records from Walvis Ridge Site 1264. *Earth and Planetary Science Letters*, *450*, 392–405. https://doi.org/10.1016/j.epsl.2016.06.007

Liebrand, D., de Bakker, A. T., Beddow, H. M., Wilson, P. A., Bohaty, S. M., Ruessink, G., et al. (2017). Evolution of the early Antarctic ice ages. *Proc Natl Acad Sci U S A*, *114*, 3867–3872. https://doi.org/10.1073/pnas.1615440114

Liu, Z., He, Y., Jiang, Y., Wang, H., Liu, W., Bohaty, S. M., & Wilson, P. A. (2018). Transient temperature asymmetry between hemispheres in the Palaeogene Atlantic Ocean. *Nature Geoscience*, *11*(9), 656–660. https://doi.org/10.1038/s41561-018-0182-9

Marino, M., Maiorano, P., Tarantino, F., Voelker, A., Capotondi, L., Girone, A., et al. (2014). Coccolithophores as proxy of seawater changes at orbital-to-millennial scale during middle Pleistocene Marine Isotope Stages 14–9 in North Atlantic core MD01-2446. *Paleoceanography and Paleoclimatology*, *29*, 518–532. https://doi.org/10.1002/2013PA002574

Mawbey, E. M., & Lear, C. H. (2013). Carbon cycle feedbacks during the Oligocene-Miocene transient glaciation. *Geology*, *41*(9), 963–966. https://doi.org/10.1130/G34422.1

McCave, I. (2008). Size sorting during transport and deposition of fine sediments: sortable silt and flow speed. *Developments in Sedimentology*, *60*, 121–142. https://doi.org/10.1016/S0070-4571(08)10008-5

McCave, I., & Tucholke, B. (1986). Deep current-controlled sedimentation in the western North Atlantic. *The Geology of North America*, *1000*, 451–468.

McCave, I. N., Manighetti, B., & Robinson, S. G. (1995). Sortable silt and fine sediment size/composition slicing: parameters for palaeo-current speed and palaeoceanography. *Paleoceanography*, *10*(3), 593–610. https://doi.org/10.1029/94PA03039

Norris, R., Wilson, P., & Blum, P. (2014). *Proceedings of the Integrated Ocean Drilling Program Exp. 342.*. College Station, TX: Integrated Ocean Drilling Program. https://doi.org/10.2204/iodp.proc.342.107.2014

Ohkouchi, N., Eglinton, T. I., Keigwin, L. D., & Hayes, J. M. (2002). Spatial and temporal offsets between proxy records in a sediment drift. *Science*, *298*(5596), 1224–1227. https://doi.org/10.1126/science.1075287

Pälike, H., Norris, R. D., Herrle, J. O., Wilson, P. A., Coxall, H. K., Lear, C. H., et al. (2006). The heartbeat of the Oligocene climate system. *Science*, *314*, 1894–1898.

Polik, C. A., Elling, F. J., & Pearson, A. (2018). Impacts of Paleoecology on the TEX86 Sea Surface Temperature Proxy in the Pliocene-Pleistocene Mediterranean Sea. *Paleoceanography and Paleoclimatology*, *33*, 1472–1489. https://doi.org/10.1029/2018PA003494

Rebesco, M., Hernández-Molina, F. J., Van Rooij, D., & Wåhlin, A. (2014). Contourites and associated sediments controlled by deep-water circulation processes: State-of-the-art and future considerations. *Marine Geology*, *352*, 111–154. https://doi.org/10.1016/j. margeo.2014.03.011

Rhein, M., Kieke, D., & Steinfeldt, R. (2015). Advection of North Atlantic Deep Water from the Labrador Sea to the southern hemisphere. *Journal of Geophysical Research: Oceans*, *120*, 2471–2487. https://doi.org/10.1002/2014JC010605

Rosell-Melé, A., & Prahl, F. G. (2013). Seasonality of UK′37 temperature estimates as inferred from sediment trap data. *Quaternary Science Reviews*, *72*, 128–136. https://doi.org/10.1016/j.quascirev.2013.04.017

Schmidt, M., Hertzberg, J., Agee, M., Bianchi, T., Marcantonio, F., Shields, M., (2018). Temporal evolution of the TEX86 export depth in the Eastern Equatorial Pacific across the last deglaciation, AGU Fall Meeting Abstracts

Schmitz, W. J., & McCartney, M. S. (1993). On the north Atlantic circulation. *Reviews of Geophysics*, *31*(1), 29–49. https://doi.org/10.1029/92RG02583

Siegel, D., & Deuser, W. (1997). Trajectories of sinking particles in the Sargasso Sea: modeling of statistical funnels above deep-ocean sediment traps. *Deep Sea Research Part I: Oceanographic Research Papers*, *44*(9-10), 1519–1541. https://doi.org/10.1016/S0967-0637(97)00028-9

Stow, D. A., Faugères, J.-C., Howe, J. A., Pudsey, C. J., & Viana, A. R. (2002). Bottom currents, contourites and deep-sea sediment drifts: current state-of-the-art. *Geological Society, London, Memoirs*, *22*(1), 7–20. https://doi.org/10.1144/GSL.MEM.2002.022.01.02

Super, J. R., Thomas, E., Pagani, M., Huber, M., O'Brien, C., & Hull, P. M. (2018). North Atlantic temperature and p CO2 coupling in the early-middle Miocene. *Geology*, *46*(6), 519–522. https://doi.org/10.1130/G40228.1

Tierney, J. E., & Tingley, M. P. (2015). A TEX(8)(6) surface sediment database and extended Bayesian calibration. *Sci Data*, *2*, 150029. https://doi.org/10.1038/sdata.2015.29

Tierney, J. E., & Tingley, M. P. (2018). BAYSPLINE: A new calibration for the alkenone paleothermometer. *Paleoceanography and Paleoclimatology*, *33*, 281–301. https://doi.org/10.1002/2017PA003201

Tremolada, F., & Bralower, T. J. (2004). Nannofossil assemblage fluctuations during the Paleocene–Eocene thermal maximum at Sites 213 (Indian Ocean) and 401 (North Atlantic Ocean): palaeoceanographic implications. *Marine Micropaleontology*, *52*(1-4), 107–116. https://doi.org/10.1016/j.marmicro.2004.04.002

Utescher, T., Dreist, A., Henrot, A.-J., Hickler, T., Liu, Y.-S. C., Mosbrugger, V., et al. (2017). Continental climate gradients in North America and Western Eurasia before and after the closure of the Central American Seaway. *Earth and Planetary Science Letters*, *472*, 120–130. https://doi.org/10.1016/j.epsl.2017.05.019

Van Peer, T. E., Liebrand, D., Xuan, C., Lippert, P. C., Agnini, C., Blum, N., et al. (2017). Data report: Revised composite depth scale and splice for IODP Site U1406. In R. D. Norris, P. A. Wilson, & P. Blum (Eds.), *Proceedings of the Integrated Ocean Drilling Program*. College Station, TX: Integrated Ocean Drilling Program. https://doi.org/10.2204/iodp.proc.342.202.2017

Van Peer, T. E., Xuan, C., Lippert, P. C., Liebrand, D., Agnini, C., & Wilson, P. A. (2017). Extracting a detailed magnetostratigraphy from weakly magnetized, Oligocene to early Miocene sediment drifts recovered at IODP Site U1406 (Newfoundland margin, northwest Atlantic Ocean). *Geochemistry, Geophysics, Geosystems*, *18*, 3910–3928. https://doi.org/10.1002/2017GC007185

Zachos, J., Pagani, M., Sloan, L., Thomas, E., & Billups, K. (2001). Trends, rhythms, and aberrations in global climate 65 Ma to present. *Science*, *292*, 686–693. https://doi.org/10.1126/science.1059412

Zhang, L., Hay, W. W., Wang, C., & Gu, X. (2019). The evolution of latitudinal temperature gradients from the latest Cretaceous through the Present. *Earth-Science Reviews*, *189*, 147–158.

Zhang, Y. G., & Liu, X. (2018). Export Depth of the TEX86 signal. *Paleoceanography and Paleoclimatology*, *33*, 666–671.

Zhang, Y. G., Pagani, M., Liu, Z., Bohaty, S. M., & Deconto, R. (2013). A 40-million-year history of atmospheric CO(2). *Philos Trans A Math Phys Eng Sci*, *371*. https://doi.org/10.1098/rsta.2013.0096